



Satellite NO₂ Retrieval Complicated by Aerosol Composition over Global Urban Agglomerations: Seasonal Variations and Long-Term Trends (2001–2018)

Song Liu, Pieter Valks, Gabriele Curci, Yuyang Chen, Lei Shu, Jianbing Jin, Shuai Sun, Dongchuan Pu, Xicheng Li, Juan Li, Xiaoxing Zuo, Weitao Fu, Yali Li, Peng Zhang, Xin Yang, Tzung-May Fu, and Lei Zhu*



Cite This: *Environ. Sci. Technol.* 2024, 58, 7891–7903



Read Online

ACCESS |

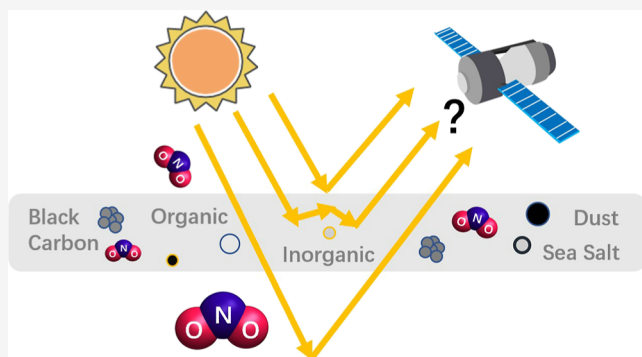
Metrics & More

Article Recommendations

Supporting Information

ABSTRACT: Tropospheric nitrogen dioxide (NO₂) poses a serious threat to the environmental quality and public health. Satellite NO₂ observations have been continuously used to monitor NO₂ variations and improve model performances. However, the accuracy of satellite NO₂ retrieval depends on the knowledge of aerosol optical properties, in particular for urban agglomerations accompanied by significant changes in aerosol characteristics. In this study, we investigate the impacts of aerosol composition on tropospheric NO₂ retrieval for an 18 year global data set from Global Ozone Monitoring Experiment (GOME)-series satellite sensors. With a focus on cloud-free scenes dominated by the presence of aerosols, individual aerosol composition affects the uncertainties of tropospheric NO₂ columns through impacts on the aerosol loading amount, relative vertical distribution of aerosol and NO₂, aerosol absorption properties, and surface albedo determination. Among aerosol compositions, secondary inorganic aerosol mostly dominates the NO₂ uncertainty by up to 43.5% in urban agglomerations, while organic aerosols contribute significantly to the NO₂ uncertainty by -8.9 to 37.3% during biomass burning seasons. The possible contrary influences from different aerosol species highlight the importance and complexity of aerosol correction on tropospheric NO₂ retrieval and indicate the need for a full picture of aerosol properties. This is of particular importance for interpreting seasonal variations or long-term trends of tropospheric NO₂ columns as well as for mitigating ozone and fine particulate matter pollution.

KEYWORDS: tropospheric NO₂, satellite remote sensing, aerosol composition, retrieval uncertainty, air quality



1. INTRODUCTION

Tropospheric nitrogen dioxide (NO₂) is an essential contributor to air pollution as a primary pollutant with adverse health outcomes^{1,2} and as a precursor to the production of ozone and fine particulate matter.³ As tropospheric NO₂ mainly arises from fossil fuel combustions, population growth and economic development in urban agglomerations have led to major NO₂ hot spots. In the past few decades, socio-economic changes have introduced a significant impact on NO₂ levels, which have been widely monitored by satellite spectrometers.^{4,5} However, such analyses may be accompanied by large variations in aerosols and potentially subject to large uncertainties as aerosol interacts with radiation and thus influences the remote sensing measurements of tropospheric NO₂. The high spatial and temporal variabilities in aerosol compositions represent complications in properly characterizing aerosol physical and optical properties, and the

comprehensive influences of aerosol components on satellite NO₂ retrieval remain unclear.

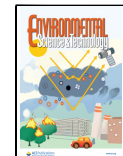
Satellite NO₂ observations started with the launch of the Global Ozone Monitoring Experiment (GOME) in 1995⁶ and have been continued by follow-up missions such as the Scanning Imaging Absorption SpectroMeter for Atmospheric CHartographY (SCIAMACHY)⁷ and the Global Ozone Monitoring Experiment-2 (GOME-2).^{8,9} This series of sensors provides continuous global measurements at nearly the same time (equator crossing time in midmorning) and has been widely used in long- and short-term NO₂ variation

Received: March 20, 2023

Revised: March 28, 2024

Accepted: March 29, 2024

Published: April 11, 2024



analysis,^{10–12} chemical model evaluations,^{13,14} and emission constraints.^{15–17}

The retrieval of the tropospheric NO₂ vertical column is implemented by dividing the tropospheric slant column by a tropospheric air mass factor (AMF). For urban agglomerations where high NO₂ and aerosol concentrations are often correlated, aerosol scattering and absorption contribute to 50% of the tropospheric AMF uncertainty.¹⁸ In current operational NO₂ products, aerosol effects can be neglected through cloud screening¹⁸ or implicitly corrected through the cloud correction, as cloud retrieval partly accounts for the aerosol effects by retrieving perturbated cloud parameters.^{19–22} However, such correction cannot fully describe the effects inherent to aerosol particles and possibly introduces significant biases to NO₂ retrieval.^{23,24}

To reduce biases related to implicit aerosol correction, research products have explicitly accounted for aerosol optical effects on regional NO₂ retrieval and found significant variations of tropospheric NO₂ columns by –70 to 90% under high aerosol loading conditions.^{25–29} Depending on the aerosol amount, scattering/absorption properties, and vertical distribution, the presence of aerosols can either increase or decrease the sensitivity of satellite NO₂ retrieval, and such effects vary strongly for different chemical compositions of aerosols. For instance, opposite effects have been noticed for regions dominated by absorbing black carbon (BC) and by scattering sulfate and organic aerosols.^{30–33}

Aerosol composition has evolved due to variations in local anthropogenic emissions associated with economic and population growth and variations in natural emissions driven by meteorological conditions.³⁴ The main goal of our study is to identify and quantify the complex influences of aerosol composition on satellite NO₂ retrieval over urban agglomerations for cloud-free aerosol-dominated scenes. Specifically, we implement a species-specific aerosol correction on GOME-type NO₂ measurements and investigate the NO₂ uncertainty changes in response to seasonal variations and long-term trends in aerosol composition. This comprehensive characterization of aerosol impacts is of particular importance for an accurate interpretation of satellite remote sensing measurements, benefiting the analysis of NO₂ spatial and temporal patterns and mitigation of ozone and fine particulate matter pollution.

2. DATA AND METHODS

2.1. GOME-Type Instruments. The GOME-type UV-visible spectrometers, GOME, SCIAMACHY, and GOME-2, fly on sun-synchronous polar orbits with local equator crossing times of 10:30, 10:00, and 9:30, respectively. GOME is a nadir-viewing instrument providing NO₂ measurements with a nominal spatial resolution of 320 × 40 km² and global coverage in 3 days from April 1996 to June 2003. SCIAMACHY delivered nadir NO₂ measurements from August 2002 until April 2012, with a spatial resolution of 60 × 30 km² and a global coverage achieved in 6 days. Finally, the GOME-2 sensor was included on MetOp-A in October 2006, MetOp-B in September 2012, and MetOp-C in November 2018. Originally, GOME-2 had an 80 × 40 km² footprint covering the Earth once every 1.5 days. In a tandem operation between MetOp-A and MetOp-B from July 2013 onward, GOME-2 on MetOp-A employs an increased spatial resolution of 40 × 40 km².

2.2. Satellite NO₂ Retrieval. The conversion between the tropospheric vertical column VCD_{tr} and the tropospheric slant column SCD_{tr} is implemented by division with tropospheric AMF M

$$VCD_{tr} = \frac{SCD_{tr}}{M} \quad (1)$$

We take SCD_{tr} from the Quality Assurance for Essential Climate Variables (QA4ECV) version 1.1 NO₂ data from GOME (January 2001 to June 2003), SCIAMACHY (August 2002 to April 2012), and GOME-2/MetOp-A (January 2007 to December 2018) data sets (<http://www.qa4ecv.eu>). Aiming at a harmonized multisensor NO₂ product, the QA4ECV project consortium generates total NO₂ slant columns based on the most recent and calibrated level 1 radiances and best-practice differential optical absorption spectroscopy fitting algorithm.^{35,36} The separation of stratospheric and tropospheric contributions to the total slant columns relies on a data assimilation approach.³⁷ The uncertainty related to the QA4ECV slant column is on average 0.8×10^{15} molecules cm⁻², and the degradation of uncertainty is relatively stable (increases by 3% yr⁻¹).³⁶ The stratospheric correction approach introduces uncertainties by up to 0.5×10^{15} molecules cm⁻².³⁷

The quality of the tropospheric NO₂ column is strongly related to tropospheric AMF M , written as the sum of altitude-dependent AMFs m_l (referred to as box-AMFs) of each layer l from the ground to the tropopause, weighted by NO₂ partial columns x_l ³⁸

$$M = \frac{\sum_l m_l(\vec{b})x_l}{\sum_l x_l} \quad (2)$$

The box-AMFs m_l are determined by a radiative transfer model, depending on a set of model parameters \vec{b} , such as satellite viewing geometry, surface albedo, and the presence of clouds and aerosols. Our AMFs are calculated using the Vector-LInearized Discrete Ordinate Radiative Transfer (VLIDORT) version 2.7 model³⁹ at 437.5 nm. Surface albedo is described by a GOME-2 Lambertian-equivalent reflectivity (LER) version 2.1 climatology.⁴⁰ *A priori* vertical profiles of aerosol extinction and NO₂ concentrations on a daily basis are from the Community Atmosphere Model with Chemistry (CAM-Chem) model simulations (for details, see Sections 2.3 and 2.4). Cloudy pixels with a cloud fraction >0.2 are excluded from the analysis.

In the framework of QA4ECV, the presence of aerosols can be considered using cloud screening, independent pixel approximation, or explicit correction.¹⁸ The cloud screening method (defined as “no aerosol correction”) assumes large uncertainties in cloud retrieval for small cloud fractions and applies the simple clear-sky AMF

$$M = M_{clr} \quad (3)$$

The independent pixel approximation (defined as “implicit aerosol correction”) is based on effective cloud parameters (assuming that cloud retrieval accounts for aerosol effects on the light path) and calculates the AMF as a linear combination of cloudy (M_{cl}) and clear (M_{clr}) components, weighted by cloud radiance fraction ω

$$M = \omega M_{cl} + (1 - \omega)M_{clr} \quad (4)$$

In our retrieval, we apply an “explicit aerosol correction” for cloud-free pure-aerosol scenarios and use the implicit aerosol correction for other partially cloudy scenes (based on consistent surface albedo and a priori NO₂ profiles). Specifically, we assume small cloud fractions (<0.1) and low cloud heights (<2 km) to be pure aerosols and no clouds, based on cloud information from the Fast Retrieval Scheme for Clouds from the Oxygen A-band (FRESCO+) algorithm.⁴¹ Similar thresholds have been widely used in previous works,^{24,27,42} and 96.7% of these scenes have nonzero aerosol optical depth (AOD) (0.41 on average) from Moderate Resolution Imaging Spectroradiometer (MODIS) Collection 6.1 (Figure S1; 10.5067/MODIS/MCD19A2CMG.061). We average the Level 3 MODIS data set (a spatial resolution of 0.05°) within each GOME-2 pixel with a cloud fraction <0.1 and a cloud height <2 km, and the availability of MODIS AOD is a good confirmation of cloud-free and aerosol-dominated scenes as MODIS AOD is retrieved exclusively for cloud-free scenes.⁴³

In the following, we focus on pure-aerosol conditions and compare the tropospheric AMFs with explicit aerosol correction to the ones without aerosol correction, which can be interpreted as the difference by which the tropospheric AMF of a clear sky should be adjusted to represent aerosol effects and can also be interpreted as the difference between cloud screening and explicit aerosol correction. For individual aerosol species, we include vertical profiles of AOD, single scattering albedo, and asymmetry parameter (for the Henyey–Greenstein phase function) in AMF calculation.

To correct for systematic biases introduced by differences in technical characteristics, calibration issues, and spatial resolutions, we apply a shift correction on tropospheric NO₂ columns from GOME, SCIAMACHY, and GOME-2.¹¹ The shift correction factors are calculated as the climatological difference between two data sets for the common period: from August 2002 to June 2003 for GOME and SCIAMACHY and from January 2007 to April 2012 for SCIAMACHY and GOME-2. The GOME-2 data set is used as a reference. Shift correction factors for the tropospheric NO₂ columns with explicit aerosol correction are shown as examples in Tables S1 and S2. Generally, low biases are noticed for GOME (up to 2.0×10^{16} molecules cm⁻²) likely as a result of coarse spatial resolution, in particular for polluted locations with inhomogeneous terrains, such as coast or valley.

2.3. CAM-Chem Model Simulations. We take vertical profiles of species-specific aerosol mass concentrations and atmospheric NO₂ concentrations from CAM-Chem (<https://rda.ucar.edu>),^{44,45} a component of the Community Earth System Model (CESM). The global simulations employ a 0.9 × 1.25° horizontal resolution with 32 vertical levels. The simulations are driven by Modern-Era Retrospective analysis for Research and Applications, version 2 (MERRA-2) meteorological fields.⁴⁶ The simulations include the new Model of Ozone and Related chemical Tracers (MOZART-T1) tropospheric chemical mechanism and the Modal Aerosol Model with 4 modes (MAM4) aerosol scheme⁴⁷ with a Volatility Basis Set (VBS) representation of secondary organic aerosol (SOA).⁴⁸ Anthropogenic emissions are taken from Copernicus Atmosphere Monitoring Service (CAMS) global anthropogenic emissions (CAMS-GLOB-ANT) version 5.1.⁴⁹ Biogenic emissions are calculated online using the Model of Emissions of Gases and Aerosols from Nature (MEGAN)

version 2.1.⁵⁰ Fire emissions are from the Quick Fire Emissions Dataset (QFED) based on observed fire detections.⁵¹

2.4. Aerosol Optical Property Calculation. We calculate layer-dependent AOD, single scattering albedo, and asymmetry parameter from CAM-Chem aerosol mass concentrations using the Flexible Aerosol Optical Depth (FlexAOD) postprocessing tool (<http://pumpkin.aquila.infn.it/flexaod>).⁵² FlexAOD was originally developed for the Goddard Earth Observing System with chemistry (GEOS-Chem) model based on the NASA Codes for Computation of Bidirectional Reflectance of Flat Particulate Layers and Rough Surfaces.⁵³ We adapt FlexAOD to CAM-Chem by matching the aerosol speciation with GEOS-Chem,⁴⁷ including secondary inorganic aerosol (SIA, containing sulfate and ammonium), primary organic matter (POM), SOA, BC, fine dust (<10 μm), and sea salt. Under the assumption of spherical particles, FlexAOD calculates aerosol optical properties based on the Mie theory.⁵⁴ All aerosol species are assumed to be distributed with a log-normal function, with the exception of dust, for which a gamma distribution is employed. Optical parameters, such as particle density, dry complex refractive index, and hygroscopic growth factor, are assigned to each aerosol species simulated by CAM-Chem (Table S3).⁵²

2.5. Evaluation of Modeled Aerosol Properties. To assess the quality of the model simulations, we compare the modeled aerosol properties with independent ground-based and space-based measurements. Specifically, we validate the modeled AOD using observations from AErosol Robotic NETwork (AERONET), known as the global ground-based network of sun-photometers (<http://aeronet.gsfc.nasa.gov>).⁵⁵ We use monthly AERONET version 3 level 2 (cloud-screened and quality-assured) data at 440 nm.⁵⁶ We select a total of 15 AERONET sites covering different dominant aerosol types, and we calculate the daytime model averages within 50 km of the sites.

Additionally, we compare the CAM-Chem aerosol vertical distribution with measurements from Cloud-Aerosol Lidar with Orthogonal Polarization (CALIOP), carried on the sun-synchronous Cloud-Aerosol Lidar and Infrared Pathfinder Satellite Observation (CALIPSO) satellite (<https://asdc.larc.nasa.gov>).⁵⁷ We use the official monthly cloud-free version 4.2 CALIOP level 3 aerosol profile product at 532 nm, which has a wide spatial coverage but a coarse horizontal resolution of 2 × 5°.⁵⁸ Moreover, we construct monthly averages on the CAM-Chem model grid (0.9 × 1.25°) based on daily version 4.2 CALIOP level 2 aerosol profile data following Liu et al.²⁸ With the above AERONET sites as representative locations, we select the closest model/CALIOP grid to the site in space, and we interpolate model results to the CALIOP overpass time (13:30 local time). As an indicator of aerosol vertical distribution, we calculate the aerosol layer height (ALH) for CAM-Chem and CALIOP data as the average height of aerosols weighted by vertically resolved aerosol extinction.^{27,28}

Finally, we evaluate the aerosol composition from CAM-Chem using filter measurements from surface particulate matter network (SPARTAN), a dedicated ground-based network with consistent instrumentation and standardized chemical analysis techniques in diverse global locations with high population densities.^{59,60} Filters sample one diurnal cycle over a 9 day period before being shipped under ambient conditions to analysis in a central laboratory. Samples were collected for 2 months to 3 years during 2013–2017 at 11 sites. The BC content is estimated based on surface reflectance

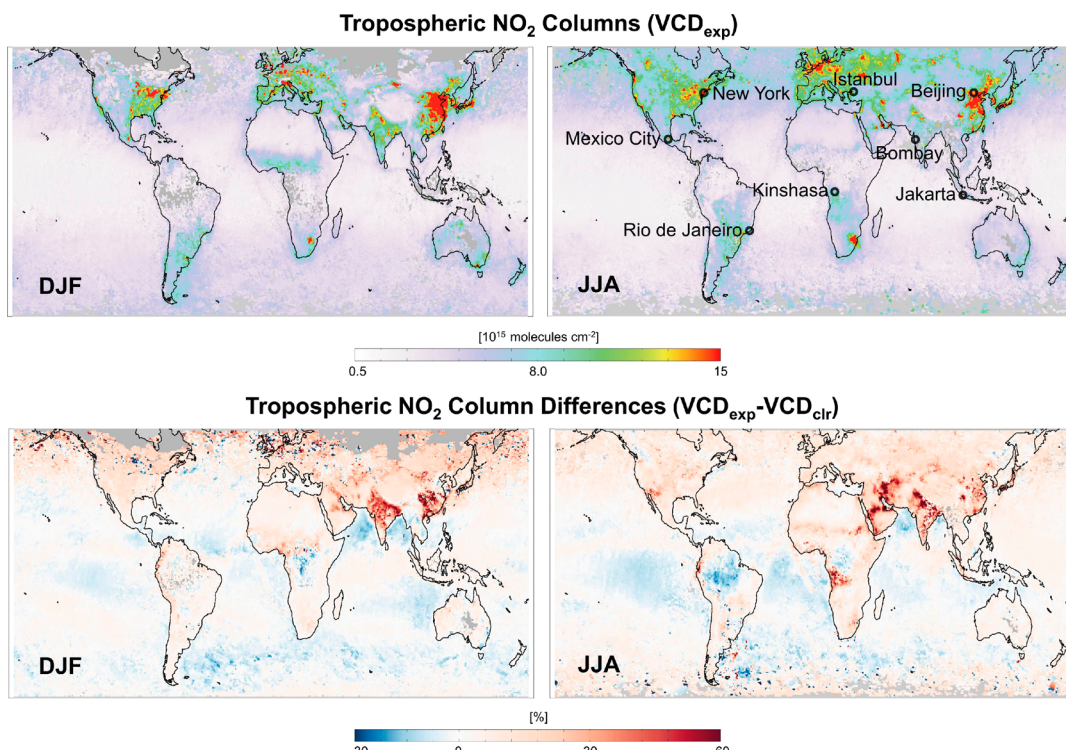


Figure 1. Seasonal mean GOME-2 tropospheric NO₂ columns retrieved with explicit aerosol correction VCD_{exp} and differences in tropospheric NO₂ columns retrieved with explicit aerosol correction and no aerosol correction (namely applying clear-sky AMFs; VCD_{exp}-VCD_{clr}) for DJF (December to February) and JJA (June to August) during 2007–2012. Black circles mark the selected urban agglomerations in Figures 2 to 4

measurements using optical rather than chemical techniques.⁶¹ The organic matter component is estimated by subtracting the dry inorganic mass and particle-bound water from the total mass.⁵⁹

As shown in Figure S2 and Table S4, the seasonal variations in AOD and ALH are similarly captured by models and observations, particularly for urban and rural regions. Biases are generally within ± 0.3 for AOD and ± 0.5 km for ALH. AOD shows a relatively compact scatter for all aerosol types with correlation coefficients between 0.34 and 0.91 (on average 0.68), while ALH presents a reduced correlation coefficient for biomass burning and dust aerosols, likely due to increased uncertainty in describing the magnitude, patterns, and drivers of biomass burning and dust emissions.^{62–64} For urban and rural scenarios, CAM-Chem shows reduced AOD (up to -0.30) and enhanced ALH (up to 0.40 km), possibly caused by the exclusion of nitrate aerosol in model simulations and the coarse resolution of the CALIOP official level 3 product, respectively. ALH calculated using the monthly level 2 data set generally shows smaller biases (ranging between -0.26 to 0.27 km; due to the improved spatial resolution) but higher standard deviations (due to the reduced data availability). In addition, the comparisons of aerosol single scattering albedo and asymmetry parameter with AERONET measurements show biases within ± 0.10 and ± 0.15 , respectively (not shown). However, the NO₂ retrieval is less sensitive to the prescribed parameters than AOD and ALH.²³

From Table S5, the simulated aerosol fractional mass agrees with SPARTAN composition measurements, with a site-averaged correlation coefficient of 0.78 for SIA (including sulfate and ammonium) and 0.72 for organic matter (including POM and SOA), suggesting CAM-Chem's skill in capturing these aerosol source contributions at the global scale. The

correlation is insignificant for BC, despite a low mean bias of -0.05 . Enhanced mean biases of fractional mass are observed for naturally derived dust (-0.11) and sea salt (0.16) components. In summary, our validation results indicate that CAM-Chem simulations are consistent with independent measurements in urban and rural scenes and are at least acceptable for biomass burning and natural sources, acting as a firm basis to provide consistent chemical and physical aerosol properties over urban agglomerations.

2.6. Evaluation of Modeled NO₂ Profile Shapes. We evaluate the modeled NO₂ profile shapes using data from airborne field campaigns and the reanalysis product. Reanalysis data are taken from the CAMS EAC4 reanalysis of NO₂ profiles at a spatial resolution of $0.75 \times 0.75^\circ$ (<https://atmosphere.copernicus.eu>).⁶⁵ In situ NO₂ profiles are gathered from the Deriving Information on Surface Conditions from Column and Vertically Resolved Observations Relevant to Air Quality (DISCOVER-AQ) campaign in the United States (<https://www-air.larc.nasa.gov/missions/discover-aq>) and the Korea–United States Air Quality Study (KORUS-AQ) campaign in South Korea (<https://www-air.larc.nasa.gov/missions/korus-aq>). During the flights, data are measured from the NASA P-3B aircraft using two different instruments: the four-channel chemiluminescence instrument from the National Center for Atmospheric Research (NCAR) and the thermal dissociation laser-induced fluorescence (TD-LIF) method.⁶⁶ Here, we average 60 s merged measurements within 1.5 h of CAM-Chem sampling time with a maximum number of data (18 UTC for DISCOVER-AQ and 00 UTC for KORUS-AQ) and interpolate CAM-Chem simulations to flight locations. We calculate a NO₂ layer height following the similar definition of ALH in Section 2.5.

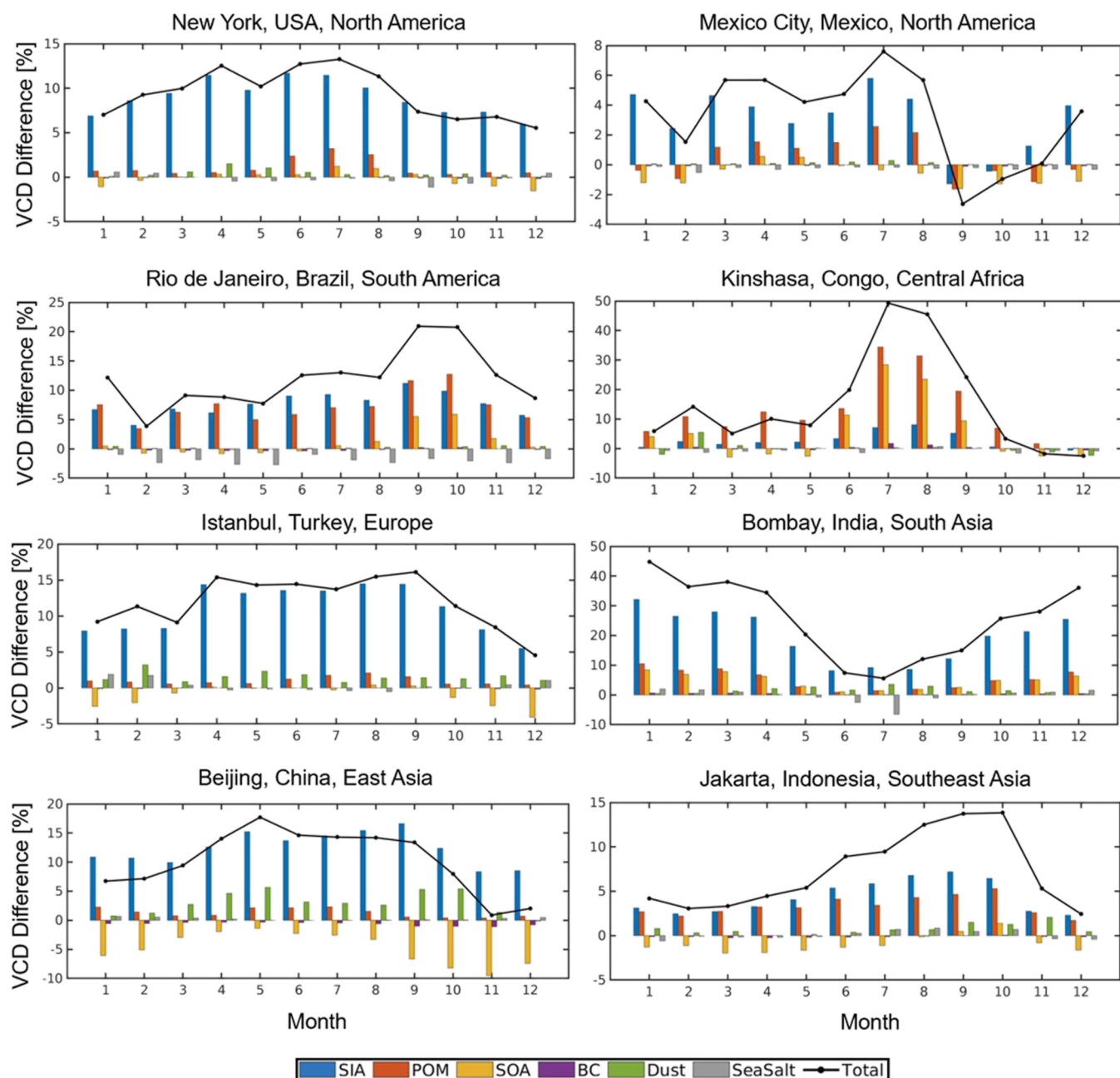


Figure 2. Monthly mean aerosol-induced NO_2 percent differences ($\text{VCD}_{\text{exp}} - \text{VCD}_{\text{clr}}$) over selected urban agglomerations during 2001–2018. Influences of total AOD (solid lines) and contributions from each aerosol species (bars) are shown. Species include SIA, POM, SOA, BC, dust, and sea salt. Satellite observations are averaged within 50 km (200 km for GOME) around the city center.

Table S6 shows the NO_2 layer heights from airborne in situ measurements, reanalysis data, and CAM-Chem simulations. Overall, the profiles generally show maximum peaks near the ground for polluted scenes, namely, the winter DISCOVER-AQ campaign in California and KORUS-AQ in the Seoul metropolitan area (Figure S3). For such shallow NO_2 layers, CAM-Chem NO_2 profiles agree with airborne measurements with an average -0.03 km bias in the NO_2 layer height. In contrast, the NO_2 layers stretch up to 2 km for summer campaigns with lower pollution levels in Colorado and Maryland, and CAM-Chem underestimates the NO_2 layer heights by up to -1.31 km. In the case of Texas with stronger land-sea breeze dynamics, the two airborne instruments show larger differences, and CAM-Chem underestimates NO_2

profiles by -0.28 km on average. Comparing to the CAMS reanalysis data, CAM-Chem simulations show better consistency with airborne measurements in polluted scenes and present larger biases for less polluted scenes. The biases are possibly related to uncertainties in emission inventories and the coarse resolution for parameterizing meteorology or chemical processes.

3. RESULTS AND DISCUSSION

Compared to the clear-sky retrieval without aerosol correction, including the explicit aerosol correction primarily affects the populated regions (Figure 1), where the urban aerosol is a complex mixture of primary particulate emissions from industry, transportation, power generation, and biomass

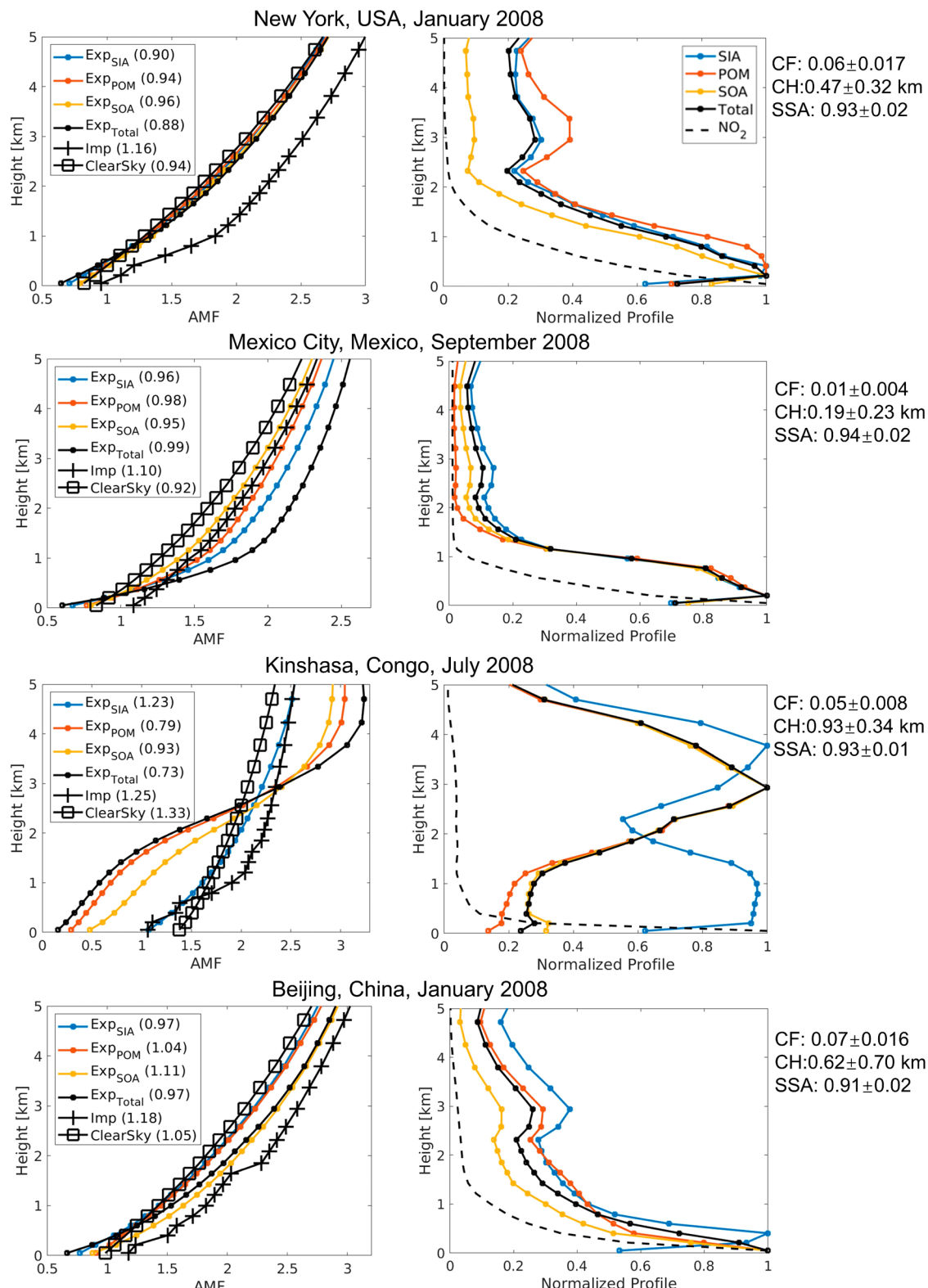


Figure 3. NO₂ box-AMFs and normalized aerosol AOD and NO₂ profiles for New York, Mexico City, Kinshasa, and Beijing. Box-AMFs are shown for explicit aerosol correction (Exp; SIA, POM, SOA, and total aerosol), implicit aerosol correction [Imp; defined as $M = \omega M_{\text{cld}} + (1 - \omega)M_{\text{clr}}$], and clear-sky retrieval (i.e., no aerosol correction). Corresponding tropospheric NO₂ AMFs are given next to each label in the legend.

burning (e.g., POM and BC) and of secondary particles formed by gas-to-particle conversion mechanisms (e.g., SIA and SOA).³ The introduction of explicit aerosol correction broadly increases the tropospheric NO₂ columns by up to about 60% for urban agglomerations in North America,

Europe, and Asia and for desert surfaces in North Africa, the Middle East, and Australia. Contrastingly, reduced NO₂ values by up to about -30% are mostly noticed over tropical countries with biomass burning activities and over the ocean with sea salt aerosol sources. The magnitudes and spatial

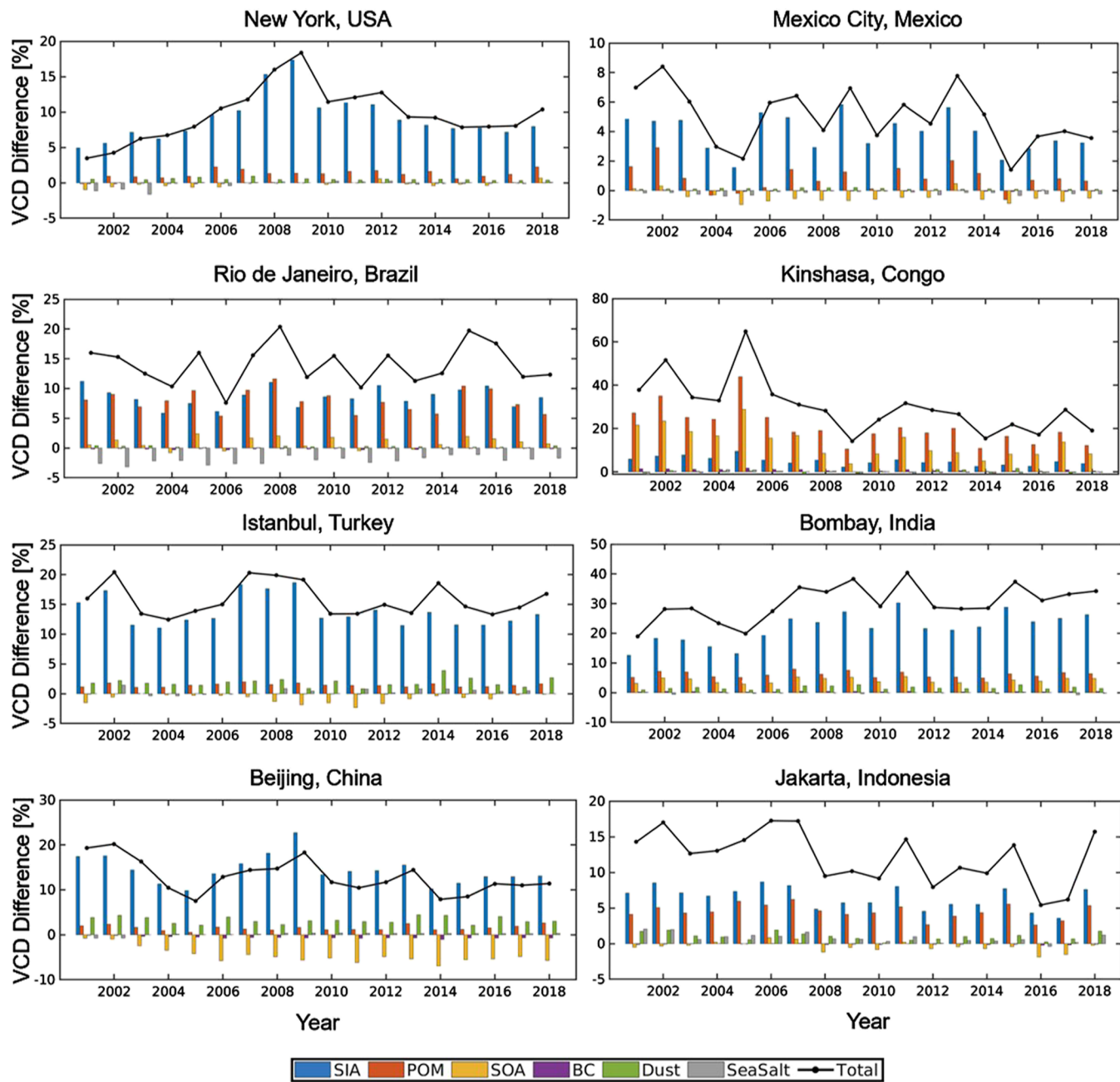


Figure 4. Same as Figure 2 but for annual mean.

patterns broadly resemble the results from previous regional studies.^{26,27}

3.1. Impact on Seasonal Variations. We implement species-specific explicit aerosol correction on GOME-type NO₂ retrieval for the 30 largest urban agglomerations ranked by population size in 2000–2035.⁶⁷ Among aerosol compositions, SIA and organic aerosols (POM and SOA) dominate aerosol light extinction (Figure S4) and thus magnitudes of NO₂ retrieval differences/uncertainties (Figure 2) for selected cases, followed by BC and naturally derived dust and sea salt. The seasonal variations of the NO₂ retrieval differences largely follow the AOD patterns, which are influenced by emission properties and meteorological conditions, such as relative humidity, precipitation, soil moisture, boundary layer height, and wind fields.

Overall, enhanced AOD (up to 0.43) and NO₂ retrieval differences (up to 15.1%) from SIA and organic aerosols are observed for New York, Istanbul, and Beijing in summer (June to August), arising from strong convection accompanied by a deeper boundary layer and hygroscopic growth of fine particles under high humidity conditions.³⁴ In contrast, high AOD (up to 0.48) and NO₂ retrieval uncertainties (up to 32.9%) in Bombay during winter (December to February) and postmonsoon (September to November) result from domestic fuel use from power generation and agricultural crop residue burning.^{68,69} Additionally, biomass burning elevates organic aerosol AOD (up to 0.93) and NO₂ retrieval uncertainties (up to 35.8%) for dry seasons in Rio de Janeiro (August to October with savanna/grassland fires), Kinshasa (June to August with woody savanna/shrubland fires), and Jakarta (June to October with forest fires).

However, seasonality from AOD and NO₂ retrieval uncertainties also exhibits disagreement, and more interestingly, NO₂ retrieval uncertainties from different aerosol species can be the opposite, likely attributed to the species-dependent differences in the vertical distribution of aerosol relative to NO₂. Taking Beijing as an example (Figure 3), while AOD for different species generally increases with decreasing altitude, a larger fraction of the SOA AOD is located near the surface due to increased precursor emissions. Consequently, NO₂ retrieval sensitivities enhance within and above the SOA layer as a result of larger scattering probability (i.e., albedo effect), increasing the tropospheric NO₂ AMF by 5.7%. More hygroscopic than SOA, SIA AOD increases with altitude below 300 m due to the higher relative humidity and enhances aloft at 3 km due to the higher aerosol hygroscopicity (corresponding to the increasing inorganic fraction of the aerosol).^{60,70} Consequently, NO₂ retrieval sensitivities reduce below the SIA aerosol layer as more photons are scattered back before reaching these altitudes (i.e., shielding effect), decreasing the tropospheric NO₂ AMF by -7.6%. Such opposite influences can also be observed, for instance, for New York with an albedo effect for SOA and shielding effect for SIA. We note here that the albedo/shielding effect can be underestimated/overestimated, considering the possible negative bias of the NO₂ layer height, as shown in Section 2.6.

Compared to Beijing or New York, the homogeneous low altitudes of SIA, POM, and SOA during rainy and cold September in Mexico City present an albedo effect for NO₂ retrieval, enhancing tropospheric AMFs by up to 6.5%. In contrast, the aerosol layers for biomass burning plumes in Kinshasa can extend to higher altitudes by up to 4 km, whereas NO₂ is in general more concentrated at lower altitudes due to a shorter lifetime, introducing a shielding effect for all SIA, POM, and SOA and reducing tropospheric NO₂ AMFs by up to -40.6%. Moreover, for places and seasons with high variability in aerosol profile shapes, e.g., Kinshasa in July, the ALH also plays an important role in explaining the generally weaker influences from total AOD than from the sum of independent contributions of each aerosol species, as shown in Figure 2. Namely, the calculation of total AOD normally smooths out the different peaks from each species, as shown in Figure 3.

3.2. Impact on Long-Term Trends. Urban agglomerations are typically sensitive to socioeconomic changes and characterized by strong variations in both tropospheric NO₂ and aerosol, particularly for aerosol loadings (Figure S5) rather than layer heights (Figure S6). Calculated with a least-squares linear regression and a trend reversal technique,¹¹ the SIA AOD (Figure S5) and SIA impacts on NO₂ retrieval (Figure 4) show decreasing trends for New York, Mexico City, Istanbul, and Beijing, particularly in the past decade with annual declines up to -0.4% yr⁻¹. This is indicative of reductions in emissions of primary anthropogenic aerosols and precursor gases associated with pollution control measures.⁷¹ Meanwhile, Beijing experiences enhancements of POM and SOA AOD, likely due to the higher emissions of biogenic and anthropogenic volatile organic compounds as well as increased atmospheric oxidizing capacity (SOA formation).^{72,73} Concerning the opposite influences from POM and SOA on NO₂ retrieval, such AOD increases are accompanied by a 0.1 and -0.2% yr⁻¹ trend of NO₂ uncertainties, respectively.

On the contrary, the homogeneous NO₂ underestimations introduced by SIA, POM, and SOA enhance annually by up to

0.6% yr⁻¹ for Bombay, related to the rapid urbanization, manufacturing, agricultural activities, and energy utilization.^{69,74} For biomass burning regions including Rio de Janeiro, Kinshasa, and Jakarta, humidity-related meteorological parameters (such as relative humidity, precipitation, and soil moisture) partly explain the interannual variations of organic aerosol effects on NO₂ retrieval (ranging between -1.1 and 0.06% yr⁻¹) under climate perturbations.³⁴

Compared to SIA and organic aerosols, BC shows minor impacts on NO₂ retrieval (e.g., up to -1.1% for Beijing in autumn) and smaller annual trends (on average -0.04% yr⁻¹ for Beijing), but such a strongly absorbing aerosol plays an important role in the determination of single scattering albedo. The increase in the aerosol-absorbing properties is accompanied by reduced single scattering albedo (up to 0.79 for Beijing), lowering the measurement sensitivities and enhancing the tropospheric NO₂ columns.³³

3.3. Implication for Global NO₂ Analysis. As a key driver of aerosol altitude and amount, Text S1 summarizes the impacts of aerosol composition on satellite NO₂ retrieval for the full list of urban agglomerations. In short, the NO₂ retrieval uncertainties are mainly contributed by SIA, in particular for East Asia and South Asia with extended urban agglomerations (up to 43.5%), and such uncertainties show upward trends with annual values up to 1.0% yr⁻¹ for South Asia. Organic aerosols dominate the NO₂ retrieval uncertainties in South America, central Africa, and Southeast Asia with intense biomass burning events (up to 37.3%). Additionally, countries such as China and India are considerably influenced by POM or SOA, with seasonal maxima ranging between -8.9 and 20.1% and long-term trends varying between -1.4 and 0.8% yr⁻¹. BC shows spatial, seasonal, and interannual patterns similar to those of SOA, although with much smaller magnitudes. Influences from the naturally derived dust aerosol on satellite NO₂ retrieval elevate by up to 8.7%, mostly in spring or summer due to the stronger vertical wind shear,⁷⁵ while impacts from sea salt mainly enhance in winter as a consequence of less wet scavenging in the drier and colder atmosphere.⁷⁶

The presence of aerosols affects the sensitivities of satellite NO₂ measurements not only directly but also indirectly through the change of surface albedo (Figure S13). Although the GOME-2 LER values are filtered for absorbing aerosols using the absorbing aerosol index measurements, persistent scattering aerosols possibly introduce an overestimation of surface albedo.⁴⁰ Such "brighter" surfaces reflect more efficiently the light back to the satellite and reduce the aerosol impacts on NO₂ retrieval.³³ Moreover, an issue not addressed in this study is the role of surface reflectance anisotropy, i.e., bidirectional reflectance distribution function (BRDF), which can be considered in NO₂ retrieval using the GOME-2 directionally dependent LER (DLER) database.⁷⁷ However, the scattering aerosols generally weaken the importance of the surface term on the radiation field and thus decrease the BRDF dependence.⁷⁸

As our study focuses on cloud-free pure-aerosol scenes, the seasonal variations and long-term trend of tropospheric NO₂ columns do not necessarily equal those of current studies including both partially cloudy and cloud-free scenes. Nevertheless, our study provides important implications for the analyses of NO₂ patterns and emission constraints. For our selected cloud-free scenes, while aerosol typically presents shielding effects (with reduced tropospheric AMFs comparing

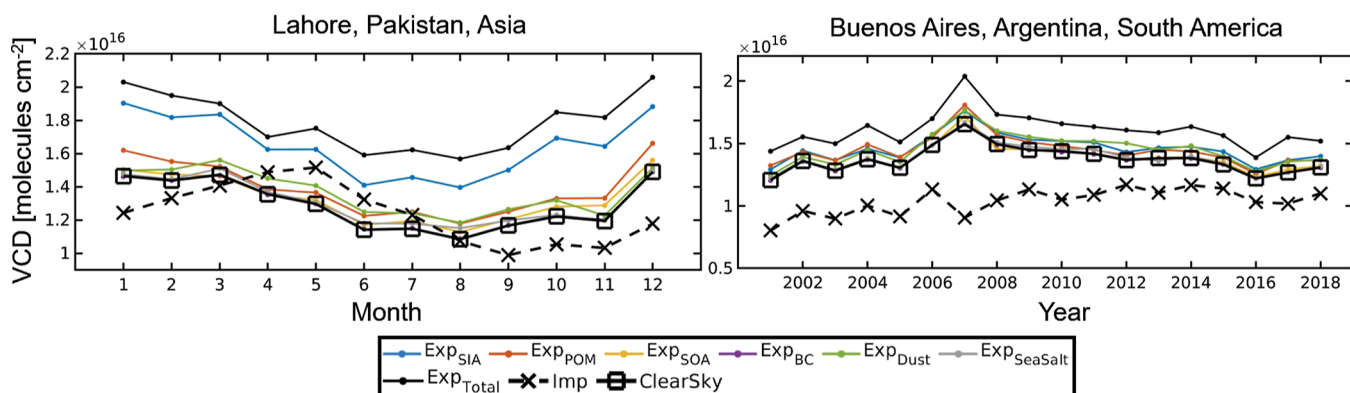


Figure 5. Seasonal variations of tropospheric NO_2 columns in Lahore and long-term trends in Buenos Aires. Results are shown for explicit aerosol correction using total AOD and species-dependent AOD (Exp), implicit aerosol correction (Imp), and clear-sky retrieval (with no aerosol correction).

to clear-sky retrieval) for urban agglomerations, such as New York and Beijing, the use of FRESCO-based implicit aerosol correction potentially overestimates tropospheric AMFs (Figure 3) and therefore underestimates tropospheric columns for elevated and high aerosol pollution, in line with previous studies.^{26,79} This is likely due to the underestimated cloud heights and thus an insufficient shielding effect applied by the implicit aerosol correction.²³ In Table S7 and Figure S14, a comparison between satellite and ground-based data in Beijing⁸⁰ confirms that using explicit aerosol correction improves the underestimation of tropospheric NO_2 columns (to -16.4%) and that implicit aerosol correction presents the largest biases (-37.7%), likely caused by the large uncertainties in effective cloud parameters for small cloud fractions and low cloud heights. Such heavily polluted site typically poses challenges for satellite validation due to the averaging of a local source over a pixel size ($80/40 \times 40 \text{ km}^2$ for GOME-2) larger than the horizontal sensitivity of the ground-based measurements (a few kilometers to tens of kilometers),^{81,82} complicated by the use of coarse-scale surface albedo and a priori NO_2 profiles in satellite retrieval. Moreover, different aerosol treatments might explain the discrepancies between satellite- and ground-based observations in urban agglomerations. As shown in Figure 5, in comparison to implicit aerosol correction, applying explicit aerosol correction or no aerosol correction better captures the winter peaks in ground-based data in SIA-dominated Lahore⁸³ and the decreasing trend in the past decade in Buenos Aires with multiple sources of aerosols.⁸⁴

Broadly following the OMI aerosol/cloud treatment scheme from Max Planck Institute for Chemistry (MPI-C; Lorente et al., 2017), our retrieval separates the GOME-2 measurements into pure aerosols (explicit correction; cloud fraction <0.1 and cloud height $<2 \text{ km}$), pure clouds (independent pixel approximation; cloud height $>3 \text{ km}$), and mixtures of aerosols and clouds, accounting for 32.9, 31.4, and 35.7% of all valid pixels with cloud fraction <0.2 , respectively. For aerosol–cloud mixtures, while MPI-C applies cloud screening, we still use the independent pixel approximation (implicit aerosol correction) as the FRESCO cloud parameters in the O_2 A band around 760 nm are less sensitive to aerosols in urban agglomerations, compared to the widely discussed O_2-O_2 cloud data at 460–490 nm.^{23,26} One reason is the wavelength dependence of the AOD value, where the AOD at 760 nm is typically a factor of 1.2–3 lower than that at 477 nm, depending on the aerosol

model.⁸⁵ Moreover, the O_2-O_2 cloud product is more sensitive to aerosols due to the application of O_2-O_2 collision-induced absorption.⁸⁶ For these aerosol–cloud mixtures, nevertheless, the retrieval of the cloud fraction and cloud height is expected to be perturbed by aerosol properties, and the complex species-dependent aerosol impacts on NO_2 retrieval will be investigated for different cloud correction models and cloud retrieval algorithms in the near future. Considering the uncertainties in cloud/aerosol correction, clear-sky AMFs are recommended to be included in satellite NO_2 products, allowing a comparison between cloud-screening and implicit aerosol correction.

For future NO_2 analysis, the continuing combustion of fossil fuel and biomass in the Indian subcontinent⁸⁷ is projected to promote the uniform NO_2 underestimation in the coming years, while the SIA reduction and SOA enhancement in Beijing^{73,88} possibly shift the underestimation of tropospheric NO_2 columns to overestimation. Moreover, events such as temperature anomaly, El Niño Southern Oscillation (ENSO), and volcanic eruptions in a changing climate significantly affect the long-term and short-term changes in aerosol loading^{34,89} and thus satellite NO_2 retrieval. The behavior of these biases could result in complex and dynamic changes in individual satellite NO_2 products. Our results point toward a necessity and challenge in improving our knowledge of aerosol composition and satellite NO_2 retrieval, which are of importance for mitigating ozone and fine particulate matter pollution.

ASSOCIATED CONTENT

Supporting Information

The Supporting Information is available free of charge at <https://pubs.acs.org/doi/10.1021/acs.est.3c02111>.

AOD observations for aerosol scenes; CAM-Chem performance evaluation; airborne NO_2 profile observations; AOD and ALH for selected urban agglomerations; summary and maps of aerosol composition impacts on urban NO_2 retrieval; aerosol-induced NO_2 retrieval differences and AOD for the full list of urban agglomerations; influence of surface albedo; validation of NO_2 retrieval; shift corrections; and optical properties in FlexAOD calculation (PDF)

AUTHOR INFORMATION

Corresponding Author

Lei Zhu — School of Environmental Science and Engineering and Shenzhen Key Laboratory of Precision Measurement and Early Warning Technology for Urban Environmental Health Risks, School of Environmental Science and Engineering, Southern University of Science and Technology, Shenzhen 518055, China; Guangdong Provincial Observation and Research Station for Coastal Atmosphere and Climate of the Greater Bay Area, Shenzhen 518055, China; Email: zhul3@sustech.edu.cn

Authors

Song Liu — School of Environmental Science and Engineering, Southern University of Science and Technology, Shenzhen 518055, China; Collaborative Innovation Center of Atmospheric Environment and Equipment Technology, Jiangsu Key Laboratory of Atmospheric Environment Monitoring and Pollution Control (AEMPC), Nanjing University of Information Science and Technology, Nanjing 210044, China; orcid.org/0000-0002-4063-0205

Pieter Valks — Institut für Methodik der Fernerkundung (IMF), Deutsches Zentrum für Luft- und Raumfahrt (DLR), Oberpfaffenhofen 82234, Germany

Gabriele Curci — Department of Physical and Chemical Sciences and Center of Excellence in Telesensing of Environment and Model Prediction of Severe Events, University of L'Aquila, L'Aquila 67100, Italy; orcid.org/0000-0001-9871-5570

Yuyang Chen — School of Environmental Science and Engineering, Southern University of Science and Technology, Shenzhen 518055, China

Lei Shu — School of Geographical Sciences, Fujian Normal University, Fuzhou 350117, China; orcid.org/0000-0002-4099-8958

Jianbing Jin — Jiangsu Key Laboratory of Atmospheric Environment Monitoring and Pollution Control, Collaborative Innovation Center of Atmospheric Environment and Equipment Technology, School of Environmental Science and Engineering, Nanjing University of Information Science and Technology, Nanjing 210044, China

Shuai Sun — School of Environmental Science and Engineering, Southern University of Science and Technology, Shenzhen 518055, China

Dongchuan Pu — School of Environmental Science and Engineering, Southern University of Science and Technology, Shenzhen 518055, China

Xicheng Li — School of Environmental Science and Engineering, Southern University of Science and Technology, Shenzhen 518055, China

Juan Li — School of Environmental Science and Engineering, Southern University of Science and Technology, Shenzhen 518055, China

Xiaoxing Zuo — School of Environmental Science and Engineering, Southern University of Science and Technology, Shenzhen 518055, China

Weitao Fu — School of Environmental Science and Engineering, Southern University of Science and Technology, Shenzhen 518055, China

Yali Li — School of Environmental Science and Engineering, Southern University of Science and Technology, Shenzhen 518055, China

Peng Zhang — School of Environmental Science and Engineering, Southern University of Science and Technology, Shenzhen 518055, China

Xin Yang — School of Environmental Science and Engineering and Shenzhen Key Laboratory of Precision Measurement and Early Warning Technology for Urban Environmental Health Risks, School of Environmental Science and Engineering, Southern University of Science and Technology, Shenzhen 518055, China; Guangdong Provincial Observation and Research Station for Coastal Atmosphere and Climate of the Greater Bay Area, Shenzhen 518055, China; orcid.org/0000-0002-9173-1188

Tzung-May Fu — School of Environmental Science and Engineering and Shenzhen Key Laboratory of Precision Measurement and Early Warning Technology for Urban Environmental Health Risks, School of Environmental Science and Engineering, Southern University of Science and Technology, Shenzhen 518055, China; Guangdong Provincial Observation and Research Station for Coastal Atmosphere and Climate of the Greater Bay Area, Shenzhen 518055, China; orcid.org/0000-0002-8556-7326

Complete contact information is available at:
<https://pubs.acs.org/10.1021/acs.est.3c02111>

Notes

The authors declare no competing financial interest.

ACKNOWLEDGMENTS

This work is funded by the National Natural Science Foundation for Young Scientists of China (42205134), Guangdong Basic and Applied Basic Research Foundation (2024A1515011951), Jiangsu Key Laboratory of Atmospheric Environment Monitoring and Pollution Control (KHK001), Shenzhen Key Laboratory of Precision Measurement and Early Warning Technology for Urban Environmental Health Risks (ZDSYS20220606100604008), Guangdong Basic and Applied Basic Research Fund (2020B1515130003), Guangdong University Research Project Science Team (2021KCXTD004), and Shenzhen Science and Technology Program (K Q T D 2 0 2 1 0 8 1 1 0 9 0 0 4 8 0 2 5 , JCYJ20210324104604012, and JCYJ20220530115404009). This work is supported by the Center for Computational Science and Engineering at Southern University of Science and Technology. We acknowledge the free use of tropospheric NO₂ column data from the GOME-SCIAMACHY-GOME-2 sensors from <https://www.temis.nl> and CAM-Chem simulation data from <https://rda.ucar.edu>. We thank all principal investigators and their staff for providing ground-based, aircraft-based, and space-based measurements of aerosol and NO₂ for validation.

REFERENCES

- (1) Hamra, G. B.; Laden, F.; Cohen, A. J.; Raaschou-Nielsen, O.; Brauer, M.; Loomis, D. Lung cancer and exposure to nitrogen dioxide and traffic: a systematic review and meta-analysis. *Environ. Health Perspect.* **2015**, *123*, 1107–1112.
- (2) Achakulwisut, P.; Brauer, M.; Hystad, P.; Anenberg, S. C. Global, national, and urban burdens of paediatric asthma incidence attributable to ambient NO₂ pollution: estimates from global datasets. *Lancet Planet Health* **2019**, *3*, e166–e178.
- (3) Seinfeld, J. H.; Pandis, S. N. *Atmospheric Chemistry and Physics: From Air Pollution to Climate Change*; John Wiley & Sons, 2016.

- (4) Shah, V.; Jacob, D. J.; Li, K.; Silvern, R. F.; Zhai, S.; Liu, M.; Lin, J.; Zhang, Q. Effect of changing NO_x lifetime on the seasonality and long-term trends of satellite-observed tropospheric NO₂ columns over China. *Atmos. Chem. Phys.* **2020**, *20*, 1483–1495.
- (5) Cooper, M. J.; Martin, R. V.; Hammer, M. S.; Levelt, P. F.; Veefkind, P.; Lamsal, L. N.; Krotkov, N. A.; Brook, J. R.; McLinden, C. A. Global fine-scale changes in ambient NO₂ during COVID-19 lockdowns. *Nature* **2022**, *601*, 380–387.
- (6) Burrows, J. P.; Weber, M.; Buchwitz, M.; Rozanov, V.; Ladstätter-Weißenmayer, A.; Richter, A.; DeBeek, R.; Hoogen, R.; Bramstedt, K.; Eichmann, K.-U.; Eisinger, M.; Perner, D. The global ozone monitoring experiment (GOME): Mission concept and first scientific results. *J. Atmos. Sci.* **1999**, *56*, 151–175.
- (7) Bovensmann, H.; Burrows, J. P.; Buchwitz, M.; Frerick, J.; Noël, S.; Rozanov, V. V.; Chance, K. V.; Goede, A. P. H. SCIAMACHY: Mission objectives and measurement modes. *J. Atmos. Sci.* **1999**, *56*, 127–150.
- (8) Callies, J.; Corpaccioli, E.; Eisinger, M.; Hahne, A.; Lefebvre, A. GOME-2-Metop's second-generation sensor for operational ozone monitoring. *ESA Bull.* **2000**, *102*, 28–36.
- (9) Munro, R.; Lang, R.; Klaes, D.; Poli, G.; Retscher, C.; Lindstrom, R.; Huckle, R.; Lacan, A.; Grzegorski, M.; Holdak, A.; Kokhanovsky, A.; Livschitz, J.; Eisinger, M. The GOME-2 instrument on the Metop series of satellites: instrument design, calibration, and level 1 data processing – an overview. *Atmos. Meas. Tech.* **2016**, *9*, 1279–1301.
- (10) Zien, A. W.; Richter, A.; Hilboll, A.; Blechschmidt, A.-M.; Burrows, J. P. Systematic analysis of tropospheric NO₂ long-range transport events detected in GOME-2 satellite data. *Atmos. Chem. Phys.* **2014**, *14*, 7367–7396.
- (11) Georgoulias, A. K.; van der A, R. J.; Stammes, P.; Boersma, K. F.; Eskes, H. J. Trends and trend reversal detection in 2 decades of tropospheric NO₂ satellite observations. *Atmos. Chem. Phys.* **2019**, *19*, 6269–6294.
- (12) Liu, S.; Valks, P.; Beirle, S.; Loyola, D. G. Nitrogen dioxide decline and rebound observed by GOME-2 and TROPOMI during COVID-19 pandemic. *Air Qual., Atmos. Health* **2021**, *14*, 1737–1755.
- (13) van Noije, T. P. C.; Eskes, H. J.; Dentener, F. J.; Stevenson, D. S.; Ellingsen, K.; Schultz, M. G.; Wild, O.; Amann, M.; Atherton, C. S.; Bergmann, D. J.; Bey, I.; Boersma, K. F.; Butler, T.; Cofala, J.; Drevet, J.; Fiore, A. M.; Gauss, M.; Hauglustaine, D. A.; Horowitz, L. W.; Isaksen, I. S. A.; Krol, M. C.; Lamarque, J.-F.; Lawrence, M. G.; Martin, R. V.; Montanaro, V.; Müller, J. F.; Pitari, G.; Prather, M. J.; Pyle, J. A.; Richter, A.; Rodriguez, J. M.; Savage, N. H.; Strahan, S. E.; Sudo, K.; Szopa, S.; van Roozendael, M. Multi-model ensemble simulations of tropospheric NO₂ compared with GOME retrievals for the year 2000. *Atmos. Chem. Phys.* **2006**, *6*, 2943–2979.
- (14) Flemming, J.; Huijnen, V.; Arteta, J.; Bechtold, P.; Beljaars, A.; Blechschmidt, A.-M.; Diamantakis, M.; Engelen, R. J.; Gaudel, A.; Inness, A.; Jones, L.; Josse, B.; Katragkou, E.; Marecal, V.; Peuch, V.-H.; Richter, A.; Schultz, M. G.; Stein, O.; Tsikkerdeksis, A. Tropospheric chemistry in the Integrated Forecasting System of ECMWF. *Geosci. Model Dev.* **2015**, *8*, 975–1003.
- (15) Gu, D.; Wang, Y.; Smeltzer, C.; Boersma, K. F. Anthropogenic emissions of NO_x over China: Reconciling the difference of inverse modeling results using GOME-2 and OMI measurements. *J. Geophys. Res.: Atmos.* **2014**, *119*, 7732–7740.
- (16) Ding, J.; Miyazaki, K.; van der A, R. J.; Mijling, B.; Kurokawa, J.-I.; Cho, S.; Janssens-Maenhout, G.; Zhang, Q.; Liu, F.; Levelt, P. F. Intercomparison of NO_x emission inventories over East Asia. *Atmos. Chem. Phys.* **2017**, *17*, 10125–10141.
- (17) Geddes, J. A.; Martin, R. V. Global deposition of total reactive nitrogen oxides from 1996 to 2014 constrained with satellite observations of NO₂ columns. *Atmos. Chem. Phys.* **2017**, *17*, 10071–10091.
- (18) Lorente, A.; Folkert Boersma, K.; Yu, H.; Dörner, S.; Hilboll, A.; Richter, A.; Liu, M.; Lamsal, L. N.; Barkley, M.; De Smedt, I.; Van Roozendael, M.; Wang, Y.; Wagner, T.; Beirle, S.; Lin, J.-T.; Krotkov, N.; Stammes, P.; Wang, P.; Eskes, H. J.; Krol, M. Structural uncertainty in air mass factor calculation for NO₂ and HCHO satellite retrievals. *Atmos. Meas. Tech.* **2017**, *10*, 759–782.
- (19) Boersma, K. F.; Eskes, H. J.; Dirksen, R. J.; van der A, R. J.; Veefkind, J. P.; Stammes, P.; Huijnen, V.; Kleipool, Q. L.; Sneep, M.; Claas, J.; Leitão, J.; Richter, A.; Zhou, Y.; Brunner, D. An improved tropospheric NO₂ column retrieval algorithm for the Ozone Monitoring Instrument. *Atmos. Meas. Tech.* **2011**, *4*, 1905–1928.
- (20) Valks, P.; Pinardi, G.; Richter, A.; Lambert, J.-C.; Hao, N.; Loyola, D.; Van Roozendael, M.; Emmadi, S. Operational total and tropospheric NO₂ column retrieval for GOME-2. *Atmos. Meas. Tech.* **2011**, *4*, 1491–1514.
- (21) Liu, S.; Valks, P.; Pinardi, G.; De Smedt, I.; Yu, H.; Beirle, S.; Richter, A. An Improved Total and Tropospheric NO₂ Column Retrieval for GOME-2. *Atmos. Meas. Tech.* **2019**, *12*, 1029–1057.
- (22) van Geffen, J.; Boersma, K. F.; Eskes, H.; Maasakers, J. D.; Veefkind, J. P. TROPOMI ATBD of the Total and Tropospheric NO₂ Data Products, 2022. SSP-KNMI-L2-0005-RP issue 2.4.0..
- (23) Chimot, J.; Vlemmix, T.; Veefkind, J. P.; de Haan, J. F.; Levelt, P. F. Impact of aerosols on the OMI tropospheric NO₂ retrievals over industrialized regions: how accurate is the aerosol correction of cloud-free scenes via a simple cloud model? *Atmos. Meas. Tech.* **2016**, *9*, 359–382.
- (24) Liu, S.; Valks, P.; Pinardi, G.; Xu, J.; Argyrouli, A.; Lutz, R.; Tilstra, L. G.; Huijnen, V.; Hendrick, F.; Van Roozendael, M. An improved air mass factor calculation for nitrogen dioxide measurements from the Global Ozone Monitoring Experiment-2 (GOME-2). *Atmos. Meas. Tech.* **2020**, *13*, 755–787.
- (25) Lin, J. T.; Martin, R. V.; Boersma, K. F.; Sneep, M.; Stammes, P.; Spurr, R.; Wang, P.; Van Roozendael, M.; Clément, K.; Irie, H. Retrieving tropospheric nitrogen dioxide from the Ozone Monitoring Instrument: effects of aerosols, surface reflectance anisotropy, and vertical profile of nitrogen dioxide. *Atmos. Chem. Phys.* **2014**, *14*, 1441–1461.
- (26) Lin, J. T.; Liu, M. Y.; Xin, J. Y.; Boersma, K. F.; Spurr, R.; Martin, R.; Zhang, Q. Influence of aerosols and surface reflectance on satellite NO₂ retrieval: seasonal and spatial characteristics and implications for NO_x emission constraints. *Atmos. Chem. Phys.* **2015**, *15*, 11217–11241.
- (27) Castellanos, P.; Boersma, K. F.; Torres, O.; De Haan, J. F. OMI tropospheric NO₂ air mass factors over South America: effects of biomass burning aerosols. *Atmos. Meas. Tech.* **2015**, *8*, 3831–3849.
- (28) Liu, M.; Lin, J.; Boersma, K. F.; Pinardi, G.; Wang, Y.; Chimot, J.; Wagner, T.; Xie, P.; Eskes, H.; Van Roozendael, M.; Hendrick, F.; Wang, P.; Wang, T.; Yan, Y.; Chen, L.; Ni, R. Improved aerosol correction for OMI tropospheric NO₂ retrieval over East Asia: constraint from CALIOP aerosol vertical profile. *Atmos. Meas. Tech.* **2019**, *12*, 1–21.
- (29) Liu, M.; Lin, J.; Kong, H.; Boersma, K. F.; Eskes, H.; Kanaya, Y.; He, Q.; Tian, X.; Qin, K.; Xie, P.; Spurr, R.; Ni, R.; Yan, Y.; Weng, H.; Wang, J. A new TROPOMI product for tropospheric NO₂ columns over East Asia with explicit aerosol corrections. *Atmos. Meas. Tech.* **2020**, *13*, 4247–4259.
- (30) Martin, R. V.; Chance, K.; Jacob, D. J.; Kurosu, T. P.; Spurr, R. J. D.; Bucsela, E.; Gleason, J. F.; Palmer, P. I.; Bey, I.; Fiore, A. M.; Li, Q.; Yantosca, R. M.; Koelemeijer, R. B. A. An improved retrieval of tropospheric nitrogen dioxide from GOME. *J. Geophys. Res.: Atmos.* **2002**, *107*, ACH 9-1–ACH 9-21.
- (31) Martin, R. V.; Jacob, D. J.; Chance, K.; Kurosu, T. P.; Palmer, P. I.; Evans, M. J. Global inventory of nitrogen oxide emissions constrained by space-based observations of NO₂ columns. *J. Geophys. Res.: Atmos.* **2003**, *108*, 4537.
- (32) Boersma, K.; Eskes, H.; Brinksma, E. Error analysis for tropospheric NO₂ retrieval from space. *J. Geophys. Res.: Atmos.* **2004**, *109*, D04311.
- (33) Leitão, J.; Richter, A.; Vrekoussis, M.; Kokhanovsky, A.; Zhang, Q.; Beekmann, M.; Burrows, J. P. On the improvement of NO₂ satellite retrievals—*aerosol impact on the airmass factors*. *Atmos. Meas. Tech.* **2010**, *3*, 475–493.

- (34) Che, H.; Gui, K.; Xia, X.; Wang, Y.; Holben, B. N.; Goloub, P.; Cuevas-Agulló, E.; Wang, H.; Zheng, Y.; Zhao, H.; Zhang, X. Large contribution of meteorological factors to inter-decadal changes in regional aerosol optical depth. *Atmos. Chem. Phys.* **2019**, *19*, 10497–10523.
- (35) Platt, U.; Stutz, J. *Differential Optical Absorption Spectroscopy*; Springer, 2008.
- (36) Zara, M.; Boersma, K. F.; De Smedt, I.; Richter, A.; Peters, E.; van Geffen, J. H. G. M.; Beirle, S.; Wagner, T.; Van Roozendael, M.; Marchenko, S.; Lamsal, L. N.; Eskes, H. J. Improved slant column density retrieval of nitrogen dioxide and formaldehyde for OMI and GOME-2A from QA4ECV: intercomparison, uncertainty characterisation, and trends. *Atmos. Meas. Tech.* **2018**, *11*, 4033–4058.
- (37) Boersma, K. F.; Eskes, H. J.; Richter, A.; De Smedt, I.; Lorente, A.; Beirle, S.; van Geffen, J. H. G. M.; Zara, M.; Peters, E.; Van Roozendael, M.; Wagner, T.; Maasakkers, J. D.; van der A, R. J.; Nightingale, J.; De Rueter, A.; Irie, H.; Pinardi, G.; Lambert, J.-C.; Compernolle, S. C. Improving algorithms and uncertainty estimates for satellite NO₂ retrievals: results from the quality assurance for the essential climate variables (QA4ECV) project. *Atmos. Meas. Tech.* **2018**, *11*, 6651–6678.
- (38) Palmer, P. I.; Jacob, D. J.; Chance, K.; Martin, R. V.; Spurr, R. J.; Kurosu, T. P.; Bey, I.; Yantosca, R.; Fiore, A.; Li, Q. Air mass factor formulation for spectroscopic measurements from satellites: Application to formaldehyde retrievals from the Global Ozone Monitoring Experiment. *J. Geophys. Res.: Atmos.* **2001**, *106*, 14539–14550.
- (39) Spurr, R. *Light Scattering Reviews* 3; Springer, 2008.
- (40) Tilstra, L.; Tuinder, O.; Wang, P.; Stammes, P. Surface reflectivity climatologies from UV to NIR determined from Earth observations by GOME-2 and SCIAMACHY. *J. Geophys. Res.: Atmos.* **2017**, *122*, 4084–4111.
- (41) Wang, P.; Stammes, P.; van der A, R.; Pinardi, G.; van Roozendael, M. FRESCO+: an improved O₂ A-band cloud retrieval algorithm for tropospheric trace gas retrievals. *Atmos. Chem. Phys.* **2008**, *8*, 6565–6576.
- (42) Jung, Y.; González Abad, G.; Nowlan, C. R.; Chance, K.; Liu, X.; Torres, O.; Ahn, C. Explicit aerosol correction of OMI formaldehyde retrievals. *Earth Space Sci.* **2019**, *6*, 2087–2105.
- (43) Remer, L. A.; Kleidman, R. G.; Levy, R. C.; Kaufman, Y. J.; Tanré, D.; Mattoe, S.; Martins, J. V.; Ichoku, C.; Koren, I.; Yu, H.; Holben, B. N. Global aerosol climatology from the MODIS satellite sensors. *J. Geophys. Res.: Atmos.* **2008**, *113*, D14S07.
- (44) Emmons, L. K.; Schwantes, R. H.; Orlando, J. J.; Tyndall, G.; Kinnison, D.; Lamarque, J.-F.; Marsh, D.; Mills, M. J.; Tilmes, S.; Bardeen, C.; Buchholz, R. R.; Conley, A.; Gettelman, A.; Garcia, R.; Simpson, I.; Blake, D. R.; Meinardi, S.; Pétron, G. The Chemistry Mechanism in the Community Earth System Model Version 2 (CESM2). *J. Adv. Model. Earth Syst.* **2020**, *12*, No. e2019MS001882.
- (45) Tilmes, S.; Emmons, L.; Buchholz, R. *The CESM2 Development Team CESM2.2/CAM-Chem Output for Boundary Conditions*; UCAR/NCAR - Atmospheric Chemistry Observations and Modeling Laboratory, 2022..
- (46) Gelaro, R.; McCarty, W.; Suárez, M. J.; Todling, R.; Molod, A.; Takacs, L.; Randles, C. A.; Darmenov, A.; Bosilovich, M. G.; Reichle, R.; Wargan, K.; Coy, L.; Cullather, R.; Draper, C.; Akella, S.; Buchard, V.; Conaty, A.; da Silva, A. M.; Gu, W.; Kim, G.-K.; Koster, R.; Lucchesi, R.; Merkova, D.; Nielsen, J. E.; Partyka, G.; Pawson, S.; Putman, W.; Riener, M.; Schubert, S. D.; Sienkiewicz, M.; Zhao, B. The modern-era retrospective analysis for research and applications, version 2 (MERRA-2). *J. Clim.* **2017**, *30*, 5419–5454.
- (47) Liu, X.; Ma, P.-L.; Wang, H.; Tilmes, S.; Singh, B.; Easter, R.; Ghan, S.; Rasch, P. Description and evaluation of a new four-mode version of the Modal Aerosol Module (MAM4) within version 5.3 of the Community Atmosphere Model. *Geosci. Model Dev.* **2016**, *9*, 505–522.
- (48) Tilmes, S.; Hodzic, A.; Emmons, L. K.; Mills, M. J.; Gettelman, A.; Kinnison, D. E.; Park, M.; Lamarque, J.-F.; Vitt, F.; Shrivastava, M.; Campuzano-Jost, P.; Jimenez, J. L.; Liu, X. Climate forcing and trends of organic aerosols in the Community Earth System Model (CESM2). *J. Adv. Model. Earth Syst.* **2019**, *11*, 4323–4351.
- (49) Granier, C.; Darras, S.; van der Gon, H. D.; Jana, D.; Elguindi, N.; Bo, G.; Michael, G.; Marc, G.; Jalkanen, J.-P.; Kuenen, J.; Lioussse, C.; Quack, B.; Simpson, D.; Sindelarova, K. *The Copernicus Atmosphere Monitoring Service Global and Regional Emissions (April 2019 Version)*; Copernicus Atmosphere Monitoring Service, 2019..
- (50) Guenther, A.; Jiang, X.; Heald, C. L.; Sakulyanontvittaya, T.; Duhl, T.; Emmons, L.; Wang, X. The Model of Emissions of Gases and Aerosols from Nature version 2.1 (MEGAN2.1): an extended and updated framework for modeling biogenic emissions. *Geosci. Model Dev.* **2012**, *5*, 1471–1492.
- (51) Koster, R. D.; Darmenov, A. S.; da Silva, A. M. *The Quick Fire Emissions Dataset (QFED): Documentation of Versions 2.1, 2.2 and 2.4*, 2015.
- (52) Curci, G.; Hogrefe, C.; Bianconi, R.; Im, U.; Balzarini, A.; Baró, R.; Brunner, D.; Forkel, R.; Giordano, L.; Hirtl, M.; Honzak, L.; Jiménez-Guerrero, P.; Knote, C.; Langer, M.; Makar, P.; Pirovano, G.; Pérez, J.; San José, R.; Syrakov, D.; Tuccella, P.; Werhahn, J.; Wolke, R.; Žabkar, R.; Zhang, J.; Galmarini, S. Uncertainties of simulated aerosol optical properties induced by assumptions on aerosol physical and chemical properties: An AQMEII-2 perspective. *Atmos. Environ.* **2015**, *115*, 541–552.
- (53) Mishchenko, M. I.; Dlugach, J. M.; Yanovitskij, E. G.; Zakharova, N. T. Bidirectional reflectance of flat, optically thick particulate layers: an efficient radiative transfer solution and applications to snow and soil surfaces. *J. Quant. Spectrosc. Radiat. Transfer* **1999**, *63*, 409–432.
- (54) Mie, G. Sättigungsstrom und Stromkurve einer schlecht leitenden Flüssigkeit. *Ann. Phys.* **1908**, *331*, 597–614.
- (55) Holben, B.; Eck, T.; Slutsker, I.; Tanré, D.; Buis, J.; Setzer, A.; Vermote, E.; Reagan, J.; Kaufman, Y.; Nakajima, T.; Lavenu, F.; Jankowiak, I.; Smirnov, A. AERONET—A federated instrument network and data archive for aerosol characterization. *Remote Sens. Environ.* **1998**, *66*, 1–16.
- (56) Sinyuk, A.; Holben, B. N.; Eck, T. F.; Giles, D. M.; Slutsker, I.; Korkin, S.; Schafer, J. S.; Smirnov, A.; Sorokin, M.; Lyapustin, A. The AERONET Version 3 aerosol retrieval algorithm, associated uncertainties and comparisons to Version 2. *Atmos. Meas. Tech.* **2020**, *13*, 3375–3411.
- (57) Winker, D.; Pelon, J.; Coakley, J. A.; Ackerman, S.; Charlson, R.; Colarco, P.; Flamant, P.; Fu, Q.; Hoff, R.; Kittaka, C.; Kubas, T. L.; Le Treut, H.; McCormick, M. P.; Mégée, G.; Poole, L.; Powell, K.; Trepte, C.; Vaughan, M. A.; Wielicki, B. A. The CALIPSO mission: A global 3D view of aerosols and clouds. *Bull. Am. Meteorol. Soc.* **2010**, *91*, 1211–1230.
- (58) Winker, D.; Tackett, J.; Getzewich, B.; Liu, Z.; Vaughan, M.; Rogers, R. The global 3-D distribution of tropospheric aerosols as characterized by CALIOP. *Atmos. Chem. Phys.* **2013**, *13*, 3345–3361.
- (59) Snider, G.; Weagle, C. L.; Martin, R. V.; van Donkelaar, A.; Conrad, K.; Cunningham, D.; Gordon, C.; Zwicker, M.; Akoshile, C.; Artaxo, P.; Anh, N. X.; Brook, J.; Dong, J.; Garland, R. M.; Greenwald, R.; Griffith, D.; He, K.; Holben, B. N.; Kahn, R.; Koren, I.; Lagrosas, N.; Lestari, P.; Ma, Z.; Vanderlei Martins, J.; Quel, E. J.; Rudich, Y.; Salam, A.; Tripathi, S. N.; Yu, C.; Zhang, Q.; Zhang, Y.; Brauer, M.; Cohen, A.; Gibson, M. D.; Liu, Y. SPARTAN: a global network to evaluate and enhance satellite-based estimates of ground-level particulate matter for global health applications. *Atmos. Meas. Tech.* **2015**, *8*, 505–521.
- (60) Weagle, C. L.; Snider, G.; Li, C.; van Donkelaar, A.; Philip, S.; Bissonnette, P.; Burke, J.; Jackson, J.; Latimer, R.; Stone, E.; Abboud, I.; Akoshile, C.; Anh, N. X.; Brook, J. R.; Cohen, A.; Dong, J.; Gibson, M. D.; Griffith, D.; He, K. B.; Holben, B. N.; Kahn, R.; Keller, C. A.; Kim, J. S.; Lagrosas, N.; Lestari, P.; Khan, Y. L.; Liu, Y.; Marais, E. A.; Martins, J. V.; Misra, A.; Muliana, U.; Pratiwi, R.; Quel, E. J.; Salam, A.; Segev, L.; Tripathi, S. N.; Wang, C.; Zhang, Q.; Brauer, M.; Rudich, Y.; Martin, R. V. Global sources of fine particulate matter: interpretation of PM_{2.5} chemical composition observed by SPARTAN

- using a global chemical transport model. *Environ. Sci. Technol.* **2018**, *52*, 11670–11681.
- (61) Quincey, P.; Butterfield, D.; Green, D.; Coyle, M.; Cape, J. N. An evaluation of measurement methods for organic, elemental and black carbon in ambient air monitoring sites. *Atmos. Environ.* **2009**, *43*, 5085–5091.
- (62) Hyer, E.; Reid, J.; Zhang, J. An over-land aerosol optical depth data set for data assimilation by filtering, correction, and aggregation of MODIS Collection 5 optical depth retrievals. *Atmos. Meas. Tech.* **2011**, *4*, 379–408.
- (63) Pan, X.; Ichoku, C.; Chin, M.; Bian, H.; Darmenov, A.; Colarco, P.; Ellison, L.; Kucsera, T.; da Silva, A.; Wang, J.; Oda, T.; Cui, G. Six global biomass burning emission datasets: intercomparison and application in one global aerosol model. *Atmos. Chem. Phys.* **2020**, *20*, 969–994.
- (64) Zhao, A.; Ryder, C. L.; Wilcox, L. J. How well do the CMIP6 models simulate dust aerosols? *Atmos. Chem. Phys.* **2022**, *22*, 2095–2119.
- (65) Inness, A.; Ades, M.; Agustí-Panareda, A.; Barré, J.; Benedictow, A.; Blechschmidt, A.-M.; Dominguez, J. J.; Engelen, R.; Eskes, H.; Flemming, J.; Huijnen, V.; Jones, L.; Kipling, Z.; Massart, S.; Parrington, M.; Peuch, V.-H.; Razinger, M.; Remy, S.; Schulz, M.; Suttie, M. The CAMS reanalysis of atmospheric composition. *Atmos. Chem. Phys.* **2019**, *19*, 3515–3556.
- (66) Choi, S.; Lamsal, L. N.; Follette-Cook, M.; Joiner, J.; Krotkov, N. A.; Swartz, W. H.; Pickering, K. E.; Loughner, C. P.; Appel, W.; Pfister, G.; Saide, P. E.; Cohen, R. C.; Weinheimer, A. J.; Herman, J. R. Assessment of NO₂ observations during DISCOVER-AQ and KORUS-AQ field campaigns. *Atmos. Meas. Tech.* **2020**, *13*, 2523–2546.
- (67) United Nations World Urbanization Prospects: The 2018 Revision. POP/DB/WUP/Rev.2018/1/F11a, 2018.
- (68) Ravindra, K.; Singh, T.; Mor, S. Emissions of air pollutants from primary crop residue burning in India and their mitigation strategies for cleaner emissions. *J. Cleaner Prod.* **2019**, *208*, 261–273.
- (69) Rawat, P.; Sarkar, S.; Jia, S.; Khillare, P. S.; Sharma, B. Regional sulfate drives long-term rise in AOD over megacity Kolkata, India. *Atmos. Environ.* **2019**, *209*, 167–181.
- (70) Liu, Q.; Quan, J.; Jia, X.; Sun, Z.; Li, X.; Gao, Y.; Liu, Y. Vertical profiles of aerosol composition over Beijing, China: Analysis of in situ aircraft measurements. *J. Atmos. Sci.* **2019**, *76*, 231–245.
- (71) Gupta, G.; Venkat Ratnam, M.; Madhavan, B.; Narayananmurthy, C. Long-term trends in Aerosol Optical Depth obtained across the globe using multi-satellite measurements. *Atmos. Environ.* **2022**, *273*, 118953.
- (72) Hu, J.; Wang, P.; Ying, Q.; Zhang, H.; Chen, J.; Ge, X.; Li, X.; Jiang, J.; Wang, S.; Zhang, J.; Zhao, Y.; Zhang, Y. Modeling biogenic and anthropogenic secondary organic aerosol in China. *Atmos. Chem. Phys.* **2017**, *17*, 77–92.
- (73) Feng, T.; Zhao, S.; Bei, N.; Wu, J.; Liu, S.; Li, X.; Liu, L.; Qian, Y.; Yang, Q.; Wang, Y.; Zhou, W.; Cao, J.; Li, G. Secondary organic aerosol enhanced by increasing atmospheric oxidizing capacity in Beijing–Tianjin–Hebei (BTH), China. *Atmos. Chem. Phys.* **2019**, *19*, 7429–7443.
- (74) Lu, Z.; Streets, D. G.; De Foy, B.; Krotkov, N. A. Ozone Monitoring Instrument observations of interannual increases in SO₂ emissions from Indian coal-fired power plants during 2005–2012. *Environ. Sci. Technol.* **2013**, *47*, 13993–14000.
- (75) Sun, H.; Liu, X.; Wang, A. Seasonal and interannual variations of atmospheric dust aerosols in mid and low latitudes of Asia—A comparative study. *Atmos. Res.* **2020**, *244*, 105036.
- (76) Pandey, S. K.; Vinoj, V.; Landu, K.; Babu, S. S. Declining pre-monsoon dust loading over South Asia: Signature of a changing regional climate. *Sci. Rep.* **2017**, *7*, 16062.
- (77) Tilstra, L. G.; Tuinder, O. N.; Wang, P.; Stammes, P. Directionally dependent Lambertian-equivalent reflectivity (DLER) of the Earth's surface measured by the GOME-2 satellite instruments. *Atmos. Meas. Tech.* **2021**, *14*, 4219–4238.
- (78) Noguchi, K.; Richter, A.; Rozanov, V.; Rozanov, A.; Burrows, J.; Irie, H.; Kita, K. Effect of surface BRDF of various land cover types on geostationary observations of tropospheric NO₂. *Atmos. Meas. Tech.* **2014**, *7*, 3497–3508.
- (79) Kanaya, Y.; Irie, H.; Takashima, H.; Iwabuchi, H.; Akimoto, H.; Sudo, K.; Gu, M.; Chong, J.; Kim, Y. J.; Lee, H.; Li, A.; Si, F.; Xu, J.; Xie, P.-H.; Liu, W.-Q.; Dzhola, A.; Postylyakov, O.; Ivanov, V.; Grechko, E.; Terpugova, S.; Panchenko, M. Long-term MAX-DOAS network observations of NO₂ in Russia and Asia (MADRAS) during the period 2007–2012: instrumentation, elucidation of climatology, and comparisons with OMI satellite observations and global model simulations. *Atmos. Chem. Phys.* **2014**, *14*, 7909–7927.
- (80) Hendrick, F.; Müller, J. F.; Clémér, K.; Wang, P.; De Mazière, M.; Fayt, C.; Gielen, C.; Hermans, C.; Ma, J. Z.; Pinardi, G.; Stavrakou, T.; Vlemmix, T.; Van Roozendael, M. Four years of ground-based MAX-DOAS observations of HONO and NO₂ in the Beijing area. *Atmos. Chem. Phys.* **2014**, *14*, 765–781.
- (81) Irie, H.; Takashima, H.; Kanaya, Y.; Boersma, K.; Gast, L.; Wittrock, F.; Brunner, D.; Zhou, Y.; Van Roozendael, M. Eight-component retrievals from ground-based MAX-DOAS observations. *Atmos. Meas. Tech.* **2011**, *4*, 1027–1044.
- (82) Ortega, I.; Koenig, T.; Sinreich, R.; Thomson, D.; Volkamer, R. The CU 2-D-MAX-DOAS instrument—Part 1: Retrieval of 3-D distributions of NO₂ and azimuth-dependent OVOC ratios. *Atmos. Meas. Tech.* **2015**, *8*, 2371–2395.
- (83) Yousaf, H.; Abbas, M.; Ghani, N.; Chaudhary, H.; Fatima, A.; Ahmad, Z.; Yasin, S. A comparative assessment of air pollutants of smog in wagah border and other sites in Lahore, Pakistan. *Braz. J. Biol.* **2024**, *84*, No. e252471.
- (84) Gómez Peláez, L. M.; Santos, J. M.; de Almeida Albuquerque, T. T.; Reis, N. C.; Andreão, W. L.; de Fátima Andrade, M. Air quality status and trends over large cities in South America. *Environ. Sci. Policy* **2020**, *114*, 422–435.
- (85) Torres, B.; Dubovik, O.; Fuertes, D.; Schuster, G.; Cachorro, V. E.; Lapyonok, T.; Goloub, P.; Blarel, L.; Barreto, A.; Mallet, M.; Toledano, C.; Tanré, D. Advanced characterisation of aerosol size properties from measurements of spectral optical depth using the GRASP algorithm. *Atmos. Meas. Tech.* **2017**, *10*, 3743–3781.
- (86) Latsch, M.; Richter, A.; Eskes, H.; Sneep, M.; Wang, P.; Veefkind, P.; Lutz, R.; Loyola, D.; Argyrouli, A.; Valks, P.; Wagner, T.; Sihler, H.; van Roozendael, M.; Theys, N.; Yu, H.; Siddans, R.; Burrows, J. P. Intercomparison of Sentinel-5P TROPOMI cloud products for tropospheric trace gas retrievals. *Atmos. Meas. Tech.* **2022**, *15*, 6257–6283.
- (87) Aas, W.; Mortier, A.; Bowersox, V.; Cherian, R.; Faluvegi, G.; Fagerli, H.; Hand, J.; Klimont, Z.; Galy-Lacaux, C.; Lehmann, C.; Myhre, C. L.; Myhre, G.; Olivie, D.; Sato, K.; Quaas, J.; Rao, P. S. P.; Schulz, M.; Shindell, D.; Skeie, R. B.; Stein, A.; Takemura, T.; Tyro, S.; Vet, R.; Xu, X.; Xu, X. Global and regional trends of atmospheric sulfur. *Sci. Rep.* **2019**, *9*, 953.
- (88) Liu, J.; Chu, B.; Chen, T.; Liu, C.; Wang, L.; Bao, X.; He, H. Secondary organic aerosol formation from ambient air at an urban site in Beijing: effects of OH exposure and precursor concentrations. *Environ. Sci. Technol.* **2018**, *52*, 6834–6841.
- (89) Ratnam, M. V.; Prasad, P.; Raj, S.; Raman, M. R.; Basha, G. Changing patterns in aerosol vertical distribution over South and East Asia. *Sci. Rep.* **2021**, *11*, 308–311.